



The Small Magellanic Cloud Investigation of Dust and Gas Evolution (SMIDGE): The Dust Extinction Curve from Red Clump Stars

Petia Yanchulova Merica-Jones¹ , Karin M. Sandstrom¹ , L. Clifton Johnson¹ , Julianne Dalcanton² , Andrew E. Dolphin³ ,
Karl Gordon^{4,5} , Julia Roman-Duval⁴ , Daniel R. Weisz⁶ , and Benjamin F. Williams²

¹ Center for Astrophysics and Space Sciences, Department of Physics, University of California, 9500 Gilman Drive, La Jolla, San Diego, CA 92093, USA

² Department of Astronomy, University of Washington, Box 351580, Seattle, WA 98195, USA

³ Raytheon, 1151 E. Hermans Road, Tucson, AZ 85756, USA

⁴ Space Telescope Science Institute, 3700 San Martin Drive, Baltimore, MD 21218, USA

⁵ Sterrenkundig Observatorium, Universiteit Gent, Gent, Belgium

⁶ Department of Astronomy, University of California, 501 Campbell Hall #3411, Berkeley, CA 94720-3411, USA

Received 2017 May 4; revised 2017 August 31; accepted 2017 September 1; published 2017 September 27

Abstract

We use *Hubble Space Telescope* (*HST*) observations of red clump stars taken as part of the Small Magellanic Cloud Investigation of Dust and Gas Evolution (SMIDGE) program to measure the average dust extinction curve in a ~ 200 pc \times 100 pc region in the southwest bar of the Small Magellanic Cloud (SMC). The rich information provided by our eight-band ultraviolet through near-infrared photometry allows us to model the color–magnitude diagram of the red clump accounting for the extinction curve shape, a log-normal distribution of A_V , and the depth of the stellar distribution along the line of sight. We measure an extinction curve with $R_{475} = A_{475}/(A_{475} - A_{814}) = 2.65 \pm 0.11$. This measurement is significantly larger than the equivalent values of published Milky Way (MW) $R_V = 3.1$ ($R_{475} = 1.83$) and SMC Bar $R_V = 2.74$ ($R_{475} = 1.86$) extinction curves. Similar extinction curve offsets in the Large Magellanic Cloud (LMC) have been interpreted as the effect of large dust grains. We demonstrate that the line-of-sight depth of the SMC (and LMC) introduces an apparent “gray” contribution to the extinction curve inferred from the morphology of the red clump. We show that no gray dust component is needed to explain extinction curve measurements when FWHM depth of 10 ± 2 kpc in the stellar distribution of the SMC (5 ± 1 kpc for the LMC) is considered, which agrees with recent studies of Magellanic Cloud stellar structure. The results of our work demonstrate the power of broadband *HST* imaging for simultaneously constraining dust and galactic structure outside the MW.

Key words: dust, extinction – galaxies: ISM – galaxies: structure – Magellanic Clouds

1. Introduction

Studying dust and its extinction is essential for our interpretation of the observational properties and evolution of galaxies. By examining dust extinction in the Small Magellanic Cloud (SMC), we can obtain a high-resolution picture of a low-metallicity environment of $1/5$ – $1/8 Z_\odot$ (Dufour 1984; Russell & Dopita 1992; Kurt et al. 1999; Rolleston et al. 1999, 2003; Lee et al. 2005) at a distance of 62 kpc (Scowcroft et al. 2016). SMC-like extinction is widely used to correct for the effects of dust in low-metallicity or high-redshift galaxies (Galliano et al. 2005; Noll & Pierini 2005; Cignoni et al. 2009; Glatt et al. 2008; Sabbi et al. 2009). Currently, however, there are only a handful of measurements of the extinction curve in the SMC.

Extinction curve measurements exist for only about 10 individual SMC sightlines toward O and B stars derived from UV spectroscopy (Lequeux et al. 1982; Prevot et al. 1984; Gordon & Clayton 1998; Gordon et al. 2003; Maíz Apellániz & Rubio 2012). These few sightlines allow only low-number statistics of extinction and dust properties in the SMC, while they also tend to probe the vicinity of star-forming regions, which may alter the dust grains in their surroundings due to the intense UV radiation fields. A more thorough appreciation of the extinction curve shape and its possible variations can be gained through large-scale multiwavelength studies, which can reveal features difficult to reliably detect by observing a handful of individual stars (e.g., Schlafly et al. 2016). To fully understand dust extinction in a low-metallicity environment, it

is therefore critical to study the SMC on a wider scale to obtain a more representative sample of extinction curves.

It is immediately clear from existing SMC extinction curve measurements that SMC-like dust is distinct from Milky Way (MW) dust. Most extinction curves in the MW are well described by an empirical relationship based on one parameter, $R_V = A_V/E(B - V) = A_V/(A_B - A_V)$, representing the ratio of total to selective extinction at optical wavelengths (Cardelli et al. 1989) and serving as a proxy for the average dust grain size along a sightline. Curves outside the Galaxy show deviations from this relationship, including all measured curves to date in the SMC (Gordon et al. 2003; Cartledge et al. 2005; Maíz Apellániz & Rubio 2012). Particular differences from MW-type dust extinction including a steeper far-UV rise and/or a weaker 2175 Å bump are evident near the 30 Doradus region in the Large Magellanic Cloud (LMC; Clayton & Martin 1985; Fitzpatrick 1985) and in the star-forming bar of the SMC (Prevot et al. 1984).

The pair method (Trumpler 1930; Massa et al. 1983; Cardelli et al. 1992) has produced the majority of extinction curves in the SMC. This method measures extinction as a function of wavelength by comparing the spectra of a reddened and an unreddened star of approximately the same spectral type. In addition to being limited to only a few lines of sight, the pair method requires high signal-to-noise ultraviolet (UV) spectroscopy, which additionally places a strict limit on the brightness of stars that can be studied. Modifications to the pair method can be made to increase the efficiency of the technique.

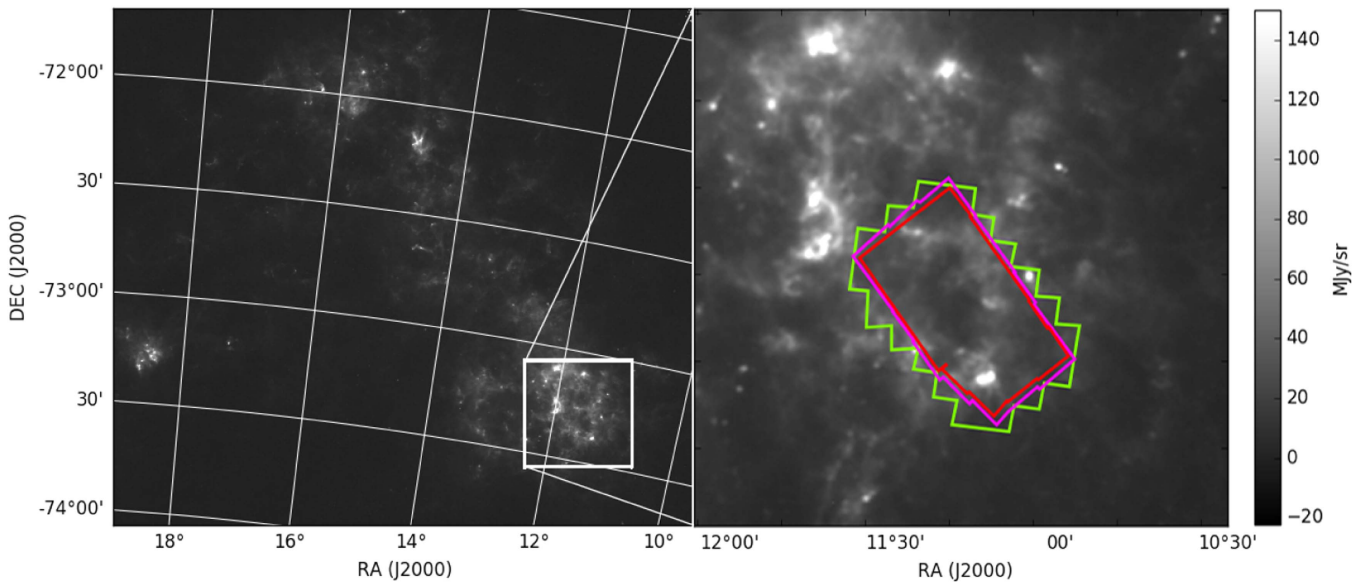


Figure 1. Location of the SMIDGE region in the southwest bar of the SMC superimposed on a *Herschel* 250 μm map. The imaging footprint of *HST*'s cameras are shown in green (ACS/WFC), magenta (WFC3/UVIS), and red (WFC3/IR).

These include using photometric measurements instead of spectroscopy and using theoretical predictions for the star's color and magnitude rather than a specific matched comparison star. In this study we use the latter approach and produce color-magnitude diagrams (CMDs) for thousands of stars, allowing us to simultaneously measure the stars' displacement due to dust from a known unreddened location. Measuring this effect, which is evident across photometric bands ranging in wavelength from UV to infrared (IR), allows us to determine the extinction curve shape.

To measure a star's displacement in CMD space due to dust extinction, we must have an idea of its initial location. The red giant clump, or red clump (RC), population is an ideal target for such techniques, due to the narrow intrinsic distribution of the stars in CMD space (Girardi & Salaris 2001; Girardi 2016). RC stars are mostly low-mass, 1–12 Gyr K giants in their He-burning phase found at the red end of the horizontal branch occupying a compact region on a CMD. Due to variable reddening by dust, the RC appears as an extended sequence stretching toward fainter magnitudes and redder colors from the unreddened RC location. By measuring the vertical displacement of the reddened RC feature, it is possible to find the dust extinction in magnitudes, A_λ . From the slope of the reddened RC, one can also measure the value of the ratio of the absolute to selective extinction, $R_\lambda = A_\lambda / (A_{\lambda'} - A_{\lambda''})$, where $A_{\lambda'} - A_{\lambda''}$ is the extinction in a chosen color combination. The selective extinction is traditionally measured in B and V filters (at 4405 and 5470 \AA), giving $A_B - A_V = E(B - V)$ and a corresponding $R_V = A_V / E(B - V)$. This technique can be applied with a variety of different color combinations to study the extinction curve shape.

The application of the RC method to measure extinction has been used in the MW (Nataf et al. 2013) and the LMC (De Marchi et al. 2014, 2016; De Marchi & Panagia 2014, hereafter DM14a, DM16, and DM14b, respectively). Some of these previous studies have led to unexpected results. DM14a first present the RC method (subsequently employed by DM14b and DM16) to study the shape of the extinction curve using multiband photometry in LMC's Tarantula Nebula. They find

R_V values of 5.6 ± 0.3 and 4.5 ± 0.2 for R136 and 30 Dor, respectively, indicating curves with a steeper optical reddening vector than the diffuse Galactic interstellar medium (ISM) of $R_V = 3.1$ (Cardelli et al. 1989) and LMC's average of $R_V = 3.4$ (Gordon et al. 2003, hereafter G03). The authors attribute this result to the presence of “gray” extinction (i.e., extinction with small changes in color). “Gray” UV/optical extinction curves with high values of R are attributed to the presence of large dust grains (Strom et al. 1971; Dunkin & Crawford 1998). Indeed, high $R_V \sim 5.5$ is observed in the dense Galactic ISM, where dust grain growth is thought to have occurred (Cardelli et al. 1989; Weingartner & Draine 2001). DM14b and DM16 argue that the observed LMC extinction curve with high R_V is indicative of large grains injected into the ISM by recent Type II supernova (SN II) explosions.

Here we present the results of a study using *Hubble Space Telescope* (*HST*) multiband observations of the SMC to characterize the average extinction curve at a range of wavelengths and over a large region of the galaxy. Our survey, named the Small Magellanic Cloud Investigation of Dust and Gas Evolution (SMIDGE), focuses on a $100 \text{ pc} \times 200 \text{ pc}$ region in the southwest bar of the SMC with observations spanning the UV to near-IR (NIR) wavelength range. Similarly to the work of DM16, we perform an analysis of *HST* observations of the 30 Doradus region in the LMC. In addition to DM16's study, we also aim to explain how the SMC's and the LMC's depth along the line of sight impacts the extinction curve shape in the region. We present the SMIDGE data in Section 2. In Section 3 we give details about how the extinction curve can be measured from RC stars and present a model of how the depth along the line of sight of the SMC impacts extinction curve measurements. In Section 4 we quantify the effect of the SMC and LMC depth along the line of sight on existing observed and model extinction curves and test the agreement between the latter and the newly derived extinction curves. We then compare our results to other extinction curve measurements. In Section 5 we discuss the significance of our results for the extinction curve shape in the SMC, and we conclude in Section 6.

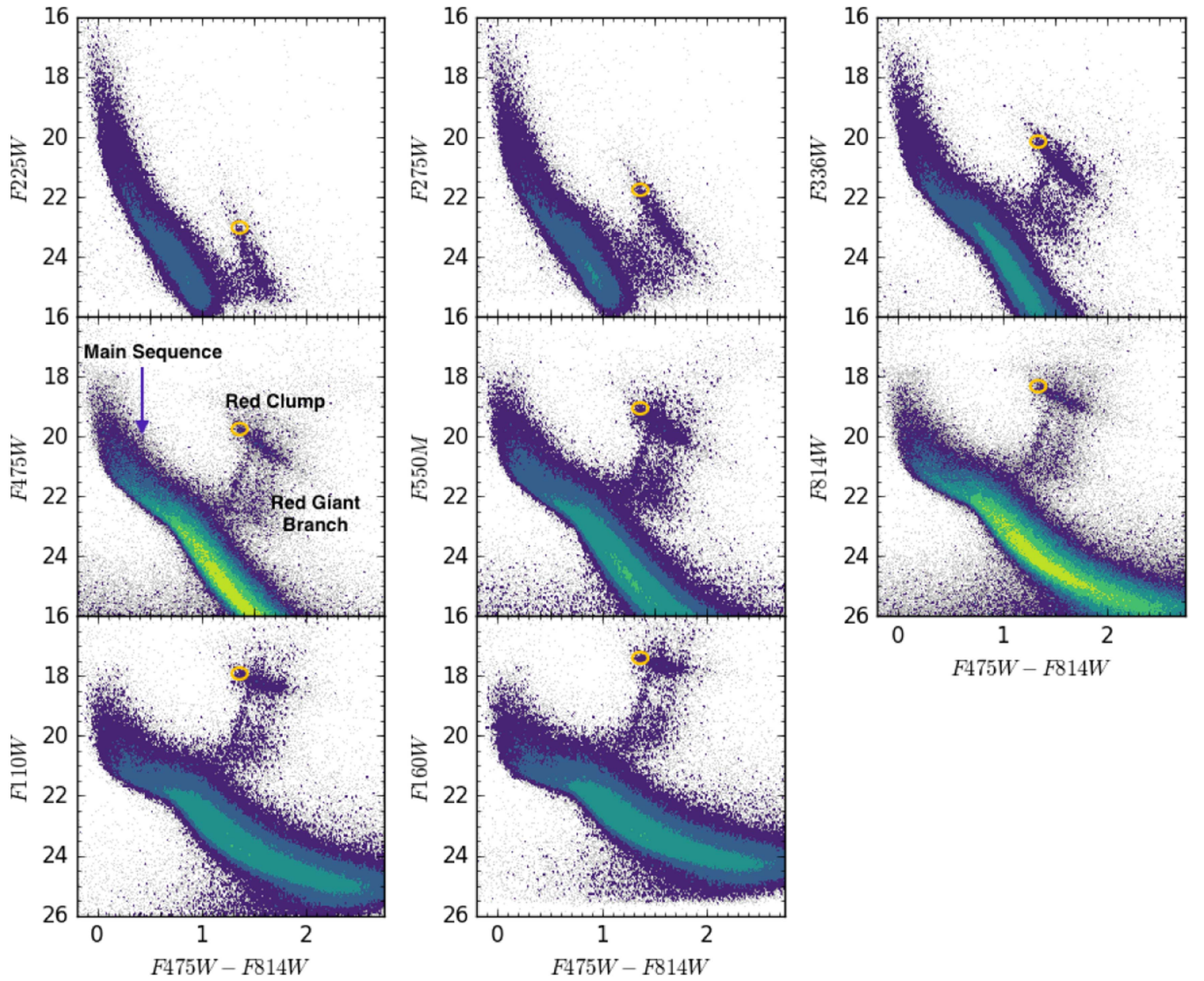


Figure 2. CMDs for the eight SMIDGE photometric bands plotted in the optical $F475W - F814W$ color after applying the culling values in Table 1. Stellar density contours range from 2 to 1200 stars decim^{-2} . The main features are shown in $F475W$'s CMD. The red clump (RC) population is seen as a streak above and somewhat parallel to the main sequence, where the orange ellipse indicates its theoretical unreddened location determined as described in Section 3.2, with values listed in Table 2. The RGB can be distinguished by its bimodal appearance rising almost vertically between the main sequence and the RC. Both the extended RC streak and the doubled RGB are consequences of dust extinction.

2. Data

We use imaging obtained by the SMIDGE survey (GO-13659) covering an area of $\sim 200 \text{ pc} \times 100 \text{ pc}$ in the southwest bar region of the SMC. The location of the imaging footprint is displayed in Figure 1. The data were obtained by the *HST*'s Advanced Camera for Surveys (ACS) Wide Field Camera (WFC) and the Wide Field Camera 3 (WFC3) instrument's IR and UV-optical (UVIS) imagers. The following broadband filters were used, covering the wavelength range $0.24\text{--}1.5 \mu\text{m}$: $F225W$, $F275W$, and $F336W$ from WFC3/UVIS; $F475W$, $F550M$, $F658N$, and $F814W$ from ACS/WFC; and $F110W$ and $F160W$ from WFC3/IR. We omit the $H\alpha$ narrowband filter $F658N$ for the purposes of this study.

We perform PSF-fitting photometry using the DOLPHOT package, an updated version of HSTPHOT (Dolphin 2000). We follow analysis procedures similar to those used by the Panchromatic Hubble Andromeda Treasury survey, as described by Williams et al. (2014). Namely, we follow the same methodologies and processing code for image alignment,

Table 1
SMIDGE Quality Cuts

Camera	Sharpness	Crowding
UVIS	0.15	1.3
ACS	0.2	2.25
IR	0.15	2.25

Note. For details see Section 2.3 of Williams et al. (2014).

cosmic-ray and artifact rejection, and DOLPHOT execution. SMIDGE processing differs in a number of ways: we use a TinyTim-based PSF library, use photometer full-depth stacks of all images simultaneously, and improve image distortion corrections. Complete details about the survey's observations, reduction, data quality, and catalog presentation will be outlined in the upcoming SMIDGE survey paper (K. M. Sandstrom et al. 2017, in preparation).

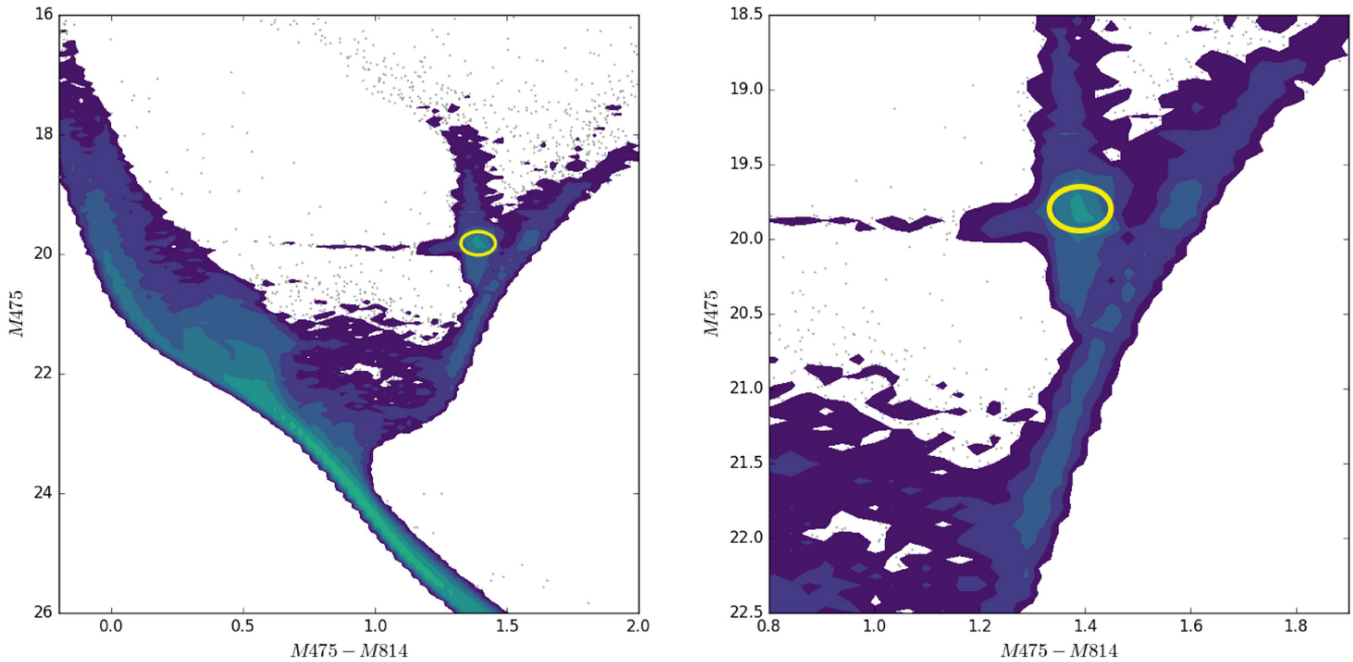


Figure 3. F475W synthetic CMD, with the unreddened RC location indicated by the yellow ellipse in both panels. The contours are logarithmic in number of stars per decimag. The selection of the unreddened RC is based on parameters specific to the SMC as explained in Section 3.2. For clarity, the width and height of the ellipse represent twice the size of the unreddened RC intrinsic spread in color and magnitude. Synthetic CMDs for the rest of the SMIDGE filters are plotted in the [Appendix](#).

We have made a number of cuts on the photometry catalogs to eliminate low-quality measurements and obtain CMDs with well-defined features. We plot the CMDs for the SMIDGE survey in Figure 2. Table 1 lists the sharpness and crowding values we have used to obtain g_{st} catalogs. We note that a red leak in *HST*'s WFC3/UV F225W affects our photometry of the RC. This is only an issue for the UV-faint RC stars in F225W, where the red leak can cause a significant offset in the photometry. Although we present the derived values of the reddening vector for F225W, we suggest caution in interpreting these values.

To analyze the extinction curve in the 30 Doradus region in the LMC, we use data from the Hubble Tarantula Treasury Project (HTTP) survey. The survey data, described in Section 2 of Sabbi et al. (2016), encompass ultraviolet to infrared wavelengths and are obtained by the *HST*'s ACS and WFC3 instruments in the set of *HST*'s F275W, F336W, F555W, F658N, F775A, F775U, F110W, and F160W filters, where F775A is ACS/WFC F775W and F775U is WFC3/UVIS F775W. We choose the ACS/WFC F775W filter, due to the larger number of sources in this passband, and we omit the narrowband filter F658N, as we do for the SMIDGE extinction curve analysis. Further survey details about the observations, data reduction and quality, and catalog presentation are discussed in Sabbi et al. (2016).

3. Extinction from Red Clump Stars

3.1. Overview

The reddened RC is prominently visible in the SMIDGE CMDs. Figure 2 shows the CMDs of the spatially resolved stars in SMIDGE's eight *HST* photometric bands using optical F475W – F814W color chosen for its best signal-to-noise ratio. In the absence of dust, the RC would be seen as a

Table 2
SMC Red Clump Properties

Filter	Theoretical RC_{Mag}	σ_{Mag}
F225W	23.22	0.21
F275W	21.83	0.15
F336W	20.32	0.11
F475W	19.78	0.09
F550W	19.22	0.09
F814W	18.40	0.09
F110W	17.96	0.09
F160W	17.44	0.09

Note. Unreddened RC location from synthetic CMD. The mean F475W – F814W color for all photometric bands is 1.38 ± 0.059 . This includes MW foreground reddening toward the SMC of $A_V = 0.18$, $R_V = 3.1$ and a distance modulus of 18.96.

compact feature on the CMD at the red end of the horizontal branch and blueward of the red giant branch (RGB). Due to variable extinction by dust, however, SMIDGE observations reveal an RC that appears as a streak above and almost parallel to the main sequence (MS), with a tail extending toward redder colors and fainter magnitudes. Since the effects of dust are great compared to the photometric uncertainty of the RC, the feature can be easily studied. To measure the extinction and extract the extinction curve slope, we measure the slope of the reddened RC streak in each CMD. The measurement requires carefully defining an unreddened RC color and magnitude, which we discuss in the next section.

Another prominent feature in the SMIDGE CMDs is the bimodal RGB. The RGB would theoretically appear as a narrow and almost vertical sequence just redward of the RC. Due to dust, however, the RGB assumes a bimodal distribution,

and this bimodality allows us to infer that the dust is in a thin layer relative to the stars. If the dust and stars were well mixed, the stellar distribution would fully sample the extinction distribution and we would see a continuously reddened RGB, which is not what we observe. Assuming that the RC and RGB stars follow the same spatial distribution, we can infer that the same bimodality should be present for the RC⁷ (i.e., a foreground unreddened population and a background reddened population). Since there are no regions in the SMIDGE field that are free from dust, we have no unreddened RC reference from our data. To accurately measure the extinction curve shape, we therefore need to rely on a model (described in the rest of Section 3) for the RC and the reddening it experiences.

3.2. A Model for the Unreddened Red Clump

We construct a model for the RC as a 2D Gaussian distribution of stars in color and magnitude. The key parameters that will set the model unreddened RC (zero-point and widths in color and magnitude) are age, metallicity, star formation history (SFH), average distance modulus, foreground reddening, and SMC depth along the line of sight. We define the RC unreddened zero-point and width by using an SFH incorporating the full ranges of ages and metallicities appropriate for the SMIDGE region. This is an improvement on previous works using this method, which use a single age and metallicity (e.g., DM14a, DM14b, and DM16). We create a simulated CMD with foreground MW extinction of $A_V = 0.18$ (derived from the MW HI foreground toward the SMIDGE field; Muller et al. 2003; Welty et al. 2012) and $R_V = 3.1$, zero line-of-sight depth, a distance modulus of 18.96 (Scowcroft et al. 2016), and an SFH based on Weisz et al. (2013), shown in Figure 3. Weisz et al. (2013) modeled the CMD of a nearby region in the SMC with similar RGB stellar surface density and with low internal dust attenuation based on deep *HST* photometry. Older populations dominating the RC are well mixed spatially, and we expect no significant difference between the Weisz et al. (2013) field and SMIDGE, except for young ages (<200 Myr). We use a simplified approximation of the SFH and age–metallicity relation (AMR), where we adopt a smooth star formation rate (SFR(t)), with SFR enhancements at 500 Myr and 1.5–3.0 Gyr and similar $Z(t)$ but offset to lower values by 0.2–0.3 dex. We compare the SMC SFH and AMR of Rubele et al. (2015) and Weisz et al. (2013) and find good consistency between the RC properties obtained from our model and from the Rubele et al. (2015) results (where higher metallicity but lower A_V and older dominant RC ages compensate). We use the `fake` CMD simulation tool (part of the `MATCH` software package; Dolphin 2002) to produce the unreddened RC model, adopting the PARSEC stellar evolution models (Bressan et al. 2012; Tang et al. 2014; Chen et al. 2015) and a Kroupa (2001) initial mass function. The match between the observed location of the unreddened RGB in SMIDGE and the synthetic RGB give us confidence in the modeled CMD. The above model allows us to account for a potentially complicated RC morphology, such as a secondary RC composed of younger stars extending toward fainter magnitudes.

We create synthetic CMDs for all F475W – F814W color–magnitude combinations. The resulting F475W CMD is plotted in

Figure 3, and the rest of the color–magnitude combinations are plotted in the Appendix. We model the position of the unreddened RC using the full stellar population in the area, which includes RC stars with a mean age of 1.81 ± 0.95 Gyr and a mean metallicity $[M/H] = -0.95 \pm 0.14$. We select RC stars in F475W – F814W matched across all eight CMDs by defining a wide box around the overdensity blueward of the RGB, from which we pick objects that fall within a density contour encompassing 70% of the total number of sources in the box. This subsample of stars has a mean age of 2.02 ± 0.66 Gyr and an average $[M/H] = -0.90 \pm 0.11$. We use the 70th percentile contour to define a mean and a standard deviation for the RC, which is represented by the yellow ellipse in Figure 3. The ellipse center is defined by measuring the centroid of the color and magnitude in the subsample in each model CMD, where the width and height of the ellipse indicate the standard deviation in color and magnitude, respectively, due to the intrinsic age and metallicity spread of the RC (Table 2). This ellipse is then used to designate the theoretical unreddened RC location in the observed CMDs. In the Appendix we examine the effects of moderate variations in the zero-point and in the width of the unreddened model RC. Effects from line-of-sight binaries are negligible due to the brightness of the RC giant primary stars. We additionally use artificial star tests to determine that the photometric error is small and therefore also negligible.

The theoretical location of the unreddened RC population is dependent on the distance to the galaxy. We adopt an average SMC distance modulus of $\mu_0 = 18.96$ mag (62 kpc) from Scowcroft et al. (2016). We test the sensitivity of our results to the assumed distance modulus in the Appendix since there is a well-known systematic distance variation as a function of position across the SMC. This variation is demonstrated by observations of Cepheid and RR Lyrae variables, supergiants, RC stars, or a combination of these populations (Florsch et al. 1981; Caldwell & Coulson 1986; Welch et al. 1987; Hatzidimitriou & Hawkins 1989; Gardiner & Hawkins 1991; Gardiner & Hatzidimitriou 1992; Subramanian & Subramanian 2009, 2012; Haschke et al. 2012; Kapakos & Hatzidimitriou 2012; Nidever et al. 2013; Jacyszyn-Dobrzniecka et al. 2016, 2017; Scowcroft et al. 2016; Subramanian et al. 2017). Several of these studies conclude that the galaxy is elongated along an axis approximately along our line of sight with a 10 kpc FWHM of the stellar density distribution (Gardiner & Hawkins 1991; Gardiner & Hatzidimitriou 1992; Nidever et al. 2013; Jacyszyn-Dobrzniecka et al. 2016; Subramanian et al. 2017). Since we extend our analysis to the LMC, we note that an LMC line-of-sight depth would similarly impact extinction curve results. For the LMC Jacyszyn-Dobrzniecka et al. (2016, hereafter JD16) conclude an FWHM distribution along the line of sight of about 5 kpc, where the LMC distance is ~ 50 kpc ($\mu_0 = 18.48 \pm 0.04$ mag; Monson et al. 2012). For both the SMC and the LMC this means that stars will have distances that vary significantly relative to the distance of the center of the galaxy itself, as illustrated in the left panel of Figure 4. This effect will inevitably be reflected on a CMD by creating a spread in the magnitude of stars.

3.3. Modeling the Reddened Red Clump

The line-of-sight depth of the SMC and the extinction the stars experience from the thin dust layer lead to an important effect: the unreddened RC stars are closer (and therefore brighter) than the reddened RC stars. An illustration of the model is given in the right panel of Figure 4. To account for all contributions to the extinction curve shape, we show the

⁷ Note that the unreddened RGB falls in the region between the unreddened and reddened RC, making it difficult to observe this bimodality.

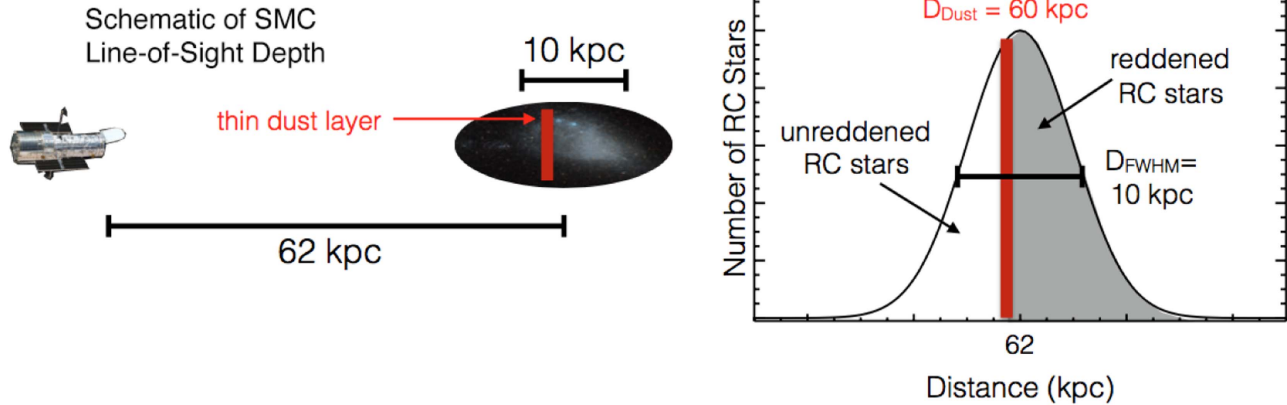


Figure 4. Example of the stellar and dust distribution in our model, with parameters corresponding to the example in Figure 5. The bimodality of the RGB leads us to conclude that the dust is located in a thin layer relative to the stars, leading to either unreddened or reddened RC stars (see Section 3.3).

combined effect of line-of-sight depth and extinction by including a thin dust layer in our model of the RC. We begin with a population of RC stars positioned at the theoretical CMD RC location described in Section 3.2. We then assume that the stars have a Gaussian distance distribution with a mean of 62 kpc average SMC distance (Scowcroft et al. 2016). In generating the model reddened RC, we convolve the initial Gaussian distribution of magnitudes for the stars with this assumed Gaussian distance distribution. As discussed in Section 3.1, we see a clear separation between the reddened and the unreddened RGB, and we can thus assume that we can neglect the dust layer’s depth along the line of sight since it is negligible compared to the depth of the distribution of the stars. The dust in our model is thus positioned in front of a fraction of the RC population, which we set at 0.65. Since this reddened fraction varies with the position of the dust relative to the stars, it is ultimately a function of the geometry of the region. Varying the fraction between 0.65 and 0.35 steepens the RC slope by 0.1–0.2 across photometric bands ranging from F160W to F225W, respectively. In a future study we plan to explore the way in which the relative geometry of the dust and stars affects the full synthetic CMD rather than only this simplified model of the RC.

The model assumes that the dust extinction experienced by the stars behind the screen has a log-normal column density distribution of A_V sampled randomly by the stars. There are several reasons for choosing a log-normal distribution (see Dalcanton et al. 2015). Observations and simulations suggest that log-normal probability density functions should be a ubiquitous feature of the turbulent ISM (Hill et al. 2008; Kainulainen et al. 2009; Hennebelle & Falgarone 2012).

Our model employs the following parameters: $\langle D \rangle$ is the mean distance to the galaxy, D_{FWHM} is the FWHM line-of-sight depth of the galaxy, the dust layer is located at a distance D_{dust} , and the stars experience a mean extinction $\langle A_V \rangle$, where the width of the log-normal distribution of extinctions is $\langle \sigma_{A_V} \rangle$. The input extinction curve slope, which corresponds to the slope of the reddening vector, is R_{in} .

To illustrate the effect of the line-of-sight depth on the measured extinction curve, we generate synthetic RC data sets using this model with an input extinction curve slope and a line-of-sight depth as in Figure 5. It is clear in panels (c) and (d) in

the figure that the line-of-sight depth causes a steepening of the reddening vector. This results from the fact that the reddened stars are more distant and therefore fainter than the unreddened stars. Panels (e) and (f) of Figure 5 show the distance modulus offset and A_V for each of the stars in the 10 kpc line-of-sight depth model depicted in panel (d). The result of the Gaussian distribution of distance moduli and the log-normal distribution of A_V is that for even the highest- A_V stars there is a range of distance moduli that, due to the Gaussian nature of the distribution, is weighted toward smaller offsets. The slope of the reddened RC is determined by the mean of this combined distribution. We also note that the theoretical, zero-depth RC ellipse is at fainter magnitudes than the observed unreddened RC. The reason for this is that the unreddened foreground RC population is closer. Nidever et al. (2013), Girardi (2016), and Subramanian et al. (2017) suggest that the effect of an extended RC seen in CMDs can be attributed to the large line-of-sight depth rather than to population effects.

3.4. Measuring the Red Clump Reddening Vector Slope

To extract the extinction curve shape from the observed CMDs, we need to determine the slope of the vector along which the RC is extended from its theoretical unreddened location. Figure 6 illustrates our technique. To find the slope of the reddening vector using the method described below, we need to first select the stars that will be used in the calculation since the extended RC is not completely isolated on the CMDs but blends into other features. We select RC stars by placing a boundary around these sources. First, we define a generous selection box surrounding the reddened RC streak. We then find the approximate slope of the reddened RC by fitting a linear slope to the points inside this region using the bisector of two lines found with the ordinary least-squares method (Isobe et al. 1990). To refine this value, we then narrow the selection region by defining upper and lower boundaries set by the width of the ellipse representing the unreddened RC and tangents to this ellipse whose slope is plus or minus 40% of the approximate slope. The bottom bound is set where the number density of sources in a region spanning one-tenth of a magnitude falls below 20 sources. We have investigated the effects of these boundary

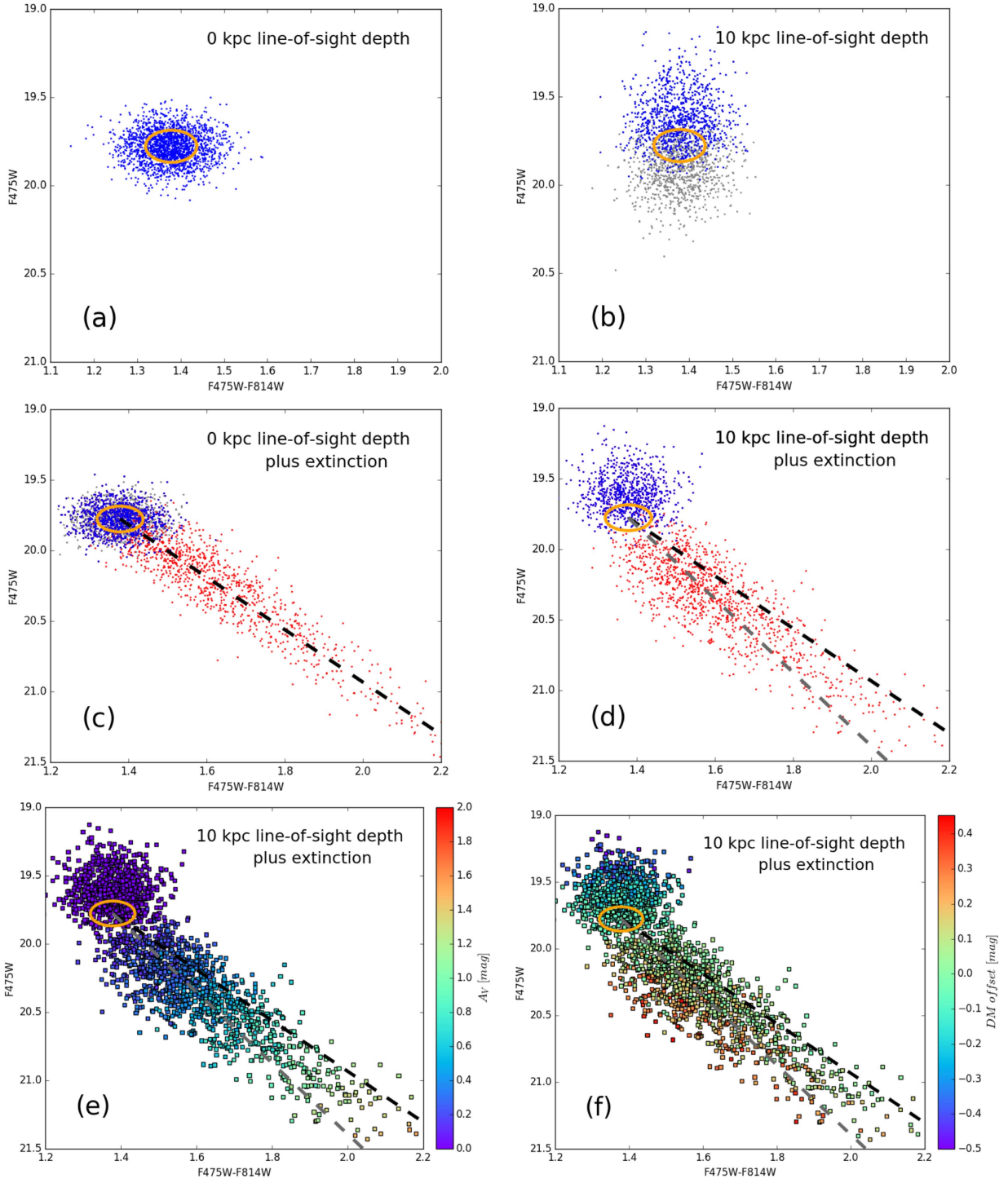


Figure 5. RC model simulating the line-of-sight depth effect. Each panel has 2000 RC stars. Panels (a) and (b) show a simulated RC population with a mean distance of $\langle D \rangle = 62$ kpc ($\mu_0 = 18.96$ mag), unaffected by dust extinction and subject to two different SMC line-of-sight depths of 0 and 10 kpc to illustrate the impact of galactic structure on the RC. Due to the highly elongated shape of the galaxy along the line of sight (as illustrated in Figure 4), stars have varying distances seen as a spread in magnitude in panel (b), where stars closer along the line of sight are in blue and stars farther along the line of sight are in gray. The orange ellipse indicates the unreddened location of the RC, with values listed in Table 2. Panels (c) and (d) show models with SMC line-of-sight depth of 0 and 10 kpc, respectively, where stars unaffected by dust remaining in the foreground are in blue and stars reddened due to dust are in red. The clump undergoes reddening with the following parameters: mean extinction in the V band of $\langle A_V \rangle = 0.4$, width of the log-normal distribution of extinction $\langle \sigma_{A_V} \rangle = 0.3$, a dust distance $D_{\text{dust}} = 60$ kpc for the 10 kpc line-of-sight depth model, and a 0.65 fraction of reddened stars. Panels (e) and (d) show models with 10 kpc line-of-sight depth where each star is color-coded by A_V and distance modulus offset. The slope of the input reddening vector, R_{in} , is indicated by the black dashed line in each plot. For comparison, the gray dashed line indicates the slope of the reddened RC with a 10 kpc line-of-sight depth as recovered from the model. For the zero line-of-sight depth case the extinction vector follows R_{in} , but for the 10 kpc line-of-sight depth case the vector is steeper since the reddened stars are farther away and therefore fainter.

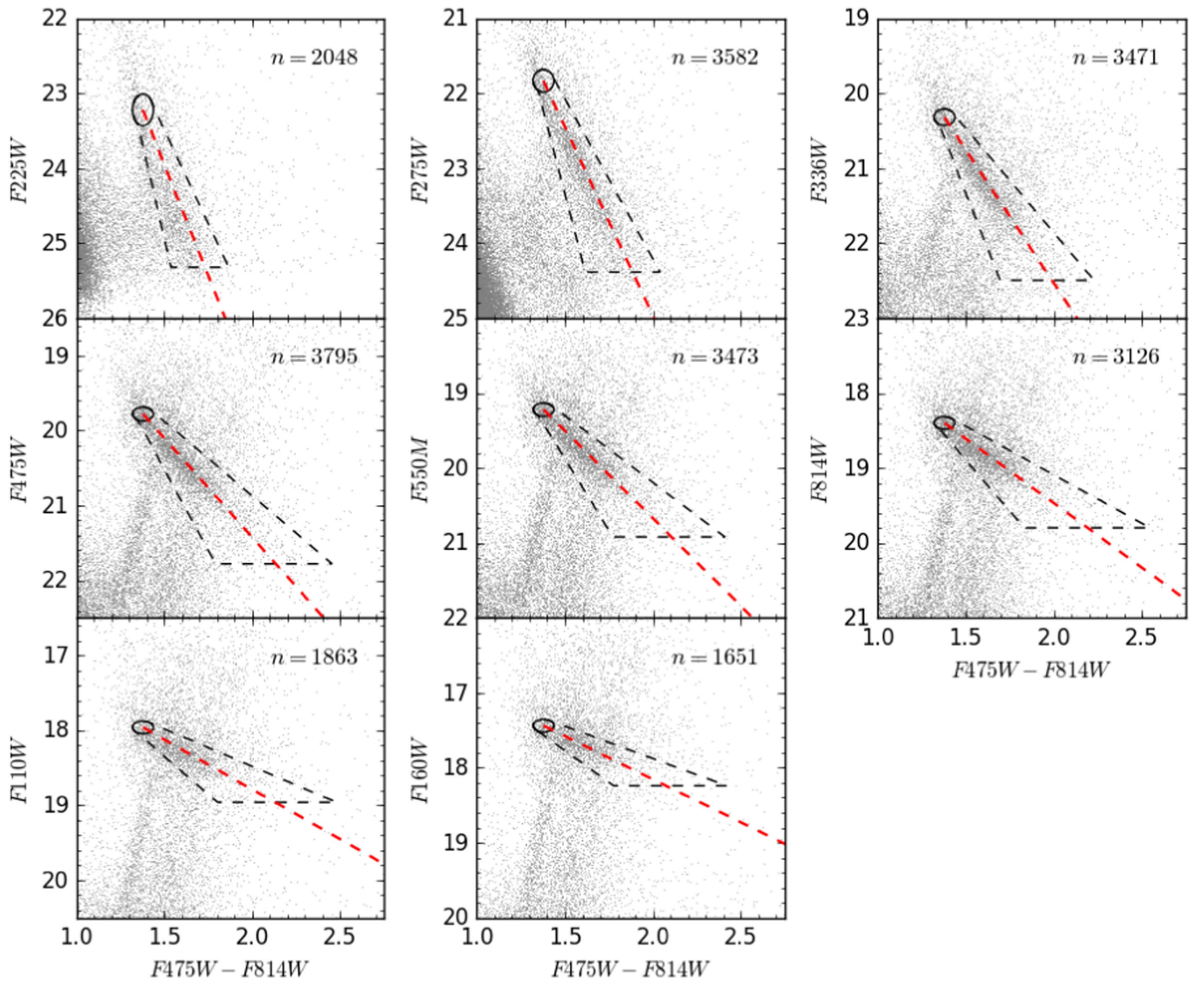


Figure 6. Selecting reddened RC stars from SMIDGE CMDs with a focus on the RC. The cone-shaped selection region is shown bound by the black dashed line. The unreddened RC appropriate to the SMC (see Section 3.2) is indicated by the black ellipse. The size of the ellipse represents the intrinsic spread in color and magnitude of the theoretical RC location due to the age range and metallicity of SMC RC stars. The red dashed line represents the calculated reddening vector obtained as described in Section 3.4, with values given in Table 4. The size of the cone is determined by the approximate slope of the reddening vector with outer boundaries obtained by multiplying this slope by a factor of 1.4 in either direction (see Section 3.4 and the Appendix). The number of sources within the selected reddened RC region is indicated by n for each photometric band.

choices on the output slope by performing a series of sensitivity tests, as described in the Appendix.

To determine the reddening, which is canonically given by $E(B - V) = A_B - A_V$, we choose *HST*'s optical F475W and F814W to obtain $E(F475W - F814W)$, resulting in $R_\lambda = A_\lambda / (A_{475} - A_{814})$. F475W and F814W have effective wavelengths of 474.7 nm and 802.4 nm, respectively, and are closely related to the Sloan Digital Sky Survey g' and Johnson-Cousins I filters with effective wavelengths of 477 nm and 806 nm, respectively (Dressel 2014). We thus approximately obtain $R_{g'I} = A_\lambda / E(g' - I)$.

The boundaries are determined independently for each combination of magnitude and $F475W - F814W$ color. Although some of the reddened sources may come from the RGB instead of strictly from the RC (see Figure 3), since they are reddened due to dust along the same vector as RC stars are,

they do not interfere with our slope measurement. We tested alternative ways to set the bounds of the RC selection, such as defining a wider or a narrower region around the apparent RC feature, extending the top and bottom bounds, or shortening the bottom bound. These variations and the results they produce are explored further in the Appendix, but they do not alter the results in addition to the reported uncertainties.

To measure the slope of the reddening vector using the refined selection of stars, we again use the bisector of the two ordinary least-squares lines. The result is the ratio of the extinction in magnitudes (absolute extinction) to that in color (selective extinction), or R_λ . The values of this vector for the range of wavelengths explored by SMIDGE produce the extinction curve itself.

Uncertainties on calculating R_λ using our method result from a combination of factors. One source of error results from the

Table 3
LMC Red Clump Properties

Filter	Theoretical RC_{Mag}	σ_{Mag}
F275W	22.20	0.12
F336W	20.34	0.12
F555W	19.16	0.08
F775W	18.21	0.08
F110W	17.72	0.10
F160W	17.15	0.10

Note. Unreddened LMC 30 Dor RC location from Girardi & Salaris (2001) and De Marchi et al. (2016, DM16), with a corresponding 1σ spread. MW foreground reddening of $E(B - V) = 0.07$ ($A_V = 0.22$) has been applied. The adopted F555W – F775W color for all photometric bands is 0.97 ± 0.12 .

intrinsic spread of the unreddened RC population caused by the range of ages and metallicities attributed to the clump. Another is due to the scatter in the RC distribution affecting the fit of the ordinary least-squares bisector line to the RC reddening vector. Since the RC becomes almost vertical in F225W’s CMD, it becomes difficult to measure the slope of the reddening vector in this filter, resulting in another source of error. All these are taken into account and are used to report the uncertainty in our results. The photometric error for these bright sources as determined using artificial star tests is small and is not taken into account. An additional systematic uncertainty in R_{225} that is not quantified results from *HST*’s F225W red leak.⁸

We perform the same analysis on data from the 30 Doradus region in the LMC from the HTTP (Sabbi et al. 2013, 2016) to compare to the DM16 extinction curve results. The HTTP survey uses observations in near-ultraviolet, optical, and NIR wavelengths in the range 0.27–1.5 μm . The unreddened locations for RC stars in the 30 Dor region are those used by DM14a based on Girardi & Salaris (2001) models, which DM14a identify (in Section 3.1 of their paper) as the RC stars with the lowest metallicity that fit the observations. To define the magnitude of the RC, they conclude a metallicity of $Z = 0.004$ for the oldest (>1 Gyr) RC stars in the 30 Dor region. To narrow down the average color for the RC, they select stars of ages 1.4–3.0 Gyr. These unreddened RC location values are listed in Table 3. The extended RC feature in the LMC CMDs is defined in the same way as the RC in the SMIDGE analysis. 30 Dor CMDs are shown in Figure 7. Since the LMC is not as deep along the line of sight as the SMC, there is less vertical spread in magnitude, which in turn allows for a clearer definition of the unreddened RC in the LMC CMDs in Figure 7. At the same time, the LMC stars studied here are much more heavily reddened than the SMC stars, and this results in an extended and noticeable reddened RC streak. LMC uncertainties in reddening vector calculations stem from similar sources to those in the SMIDGE analysis discussed above. In our final analysis we calculate the slope for six LMC photometric bands: F275W, F336W, F555W, F775W, F775U, F110W, and F160W.

3.5. Results

R_λ results for the SMC and LMC are given in Tables 4 and 5, respectively. We plot the extinction curves in Figure 8 along with other known extinction curves for comparison, such

⁸ The red leak affects the measured stellar magnitudes in F225W by contributing to an off-band flux in the red part of the spectrum (Dressel 2014).

as those of G03 and Fitzpatrick (1999, hereafter F99). Our results for the LMC are in good agreement with the results of DM16. For both the SMC and LMC we observe a larger R_λ than indicated by existing spectroscopic extinction curve measurements. For comparison, the new SMC extinction curve has $R_{475} = A_{475}/(A_{475} - A_{814}) = 2.65 \pm 0.11$, while the G03 equivalents are $R_{475}^{SMCbar} = 1.86$ and $R_{475}^{SMCwing} = 1.57$, and the F99 MW $R_V = 3.1$ equivalent is $R_{475}^{MW} = 1.83$. The LMC extinction curve we measure has $R_{555} = A_{555}/(A_{555} - A_{775}) = 3.16 \pm 0.3$, while the G03 equivalents are $R_{555}^{LMCave} = 2.48$ and $R_{555}^{LMC2} = 2.61$, and the F99 MW $R_V = 3.1$ equivalent is $R_{555}^{MW} = 2.37$. In the section that follows we discuss the interpretation of these measurements in light of recent observations that both the SMC and the LMC have a substantial line-of-sight depth, which significantly impacts the calculations.

4. Interpreting Extinction Results

4.1. Line-of-sight Depth Effect on Model Extinction Curves

We use our reddened RC model to determine what the line-of-sight depth impact would be on SMC and LMC extinction curves observed by G03 and modeled by Weingartner & Draine (2001, hereafter WD01), as well as the F99 model MW curves. We begin by taking the R_λ value of an observed or modeled extinction curve as an input extinction curve slope R_{in} for the RC model. The unreddened RC locations are those specified in Tables 2 and 3. We then apply the procedure described in Section 3.3, while we vary the line-of-sight depth between 0 and 15 kpc to extract an output slope R_{out} . The results plotted in Figure 9 indicate that an increasing depth along the line of sight steepens the reddening vector slope such that the extinction curve produced as a result experiences an offset toward higher R_λ .

As shown by the monotonic increase in R_{out} with depth, the line-of-sight depth effect is color independent to first order in that all wavelengths are affected by the extended structure along the line of sight approximately equally. Essentially, the line-of-sight depth means that the reddened RC stars are farther away than the theoretical zero-point would suggest, leading to the reddened stars being offset to fainter magnitudes. In essence, distance offsets are mimicking a truly “gray” extinction curve. This fact allows us to separate the distance effect from the effect of extinction by dust. However, our sensitivity tests, described in the Appendix, illustrate that the assumed average RC distance modulus is somewhat degenerate, with the line-of-sight depth shown in Figure 9. In the sensitivity tests we move the RC zero-points for all filter combinations by ± 0.15 mag, which in effect shifts the average distance of the RC stellar distribution by ± 4.5 kpc (we note that this is well outside the measured uncertainty of the average distance to the SMC; Scowcroft et al. 2016). The shift in R_{out} introduced by this offset is color independent to first order, as is the line-of-sight depth effect. We find that a $+0.15$ mag shift in the RC zero-point would lead to a line-of-sight depth measurement of ~ 7 kpc, rather than 10 kpc, and a -0.15 mag shift leads to an even larger line-of-sight depth. This test shows that for a reasonable range of SMC distance moduli, explaining our measured reddening vector slopes necessitates a large line-of-sight depth.

To test the degree of agreement between the resulting SMC SMIDGE region extinction curve and the extinction curves of G03, F99, and WD01, and to extract the line-of-sight depth

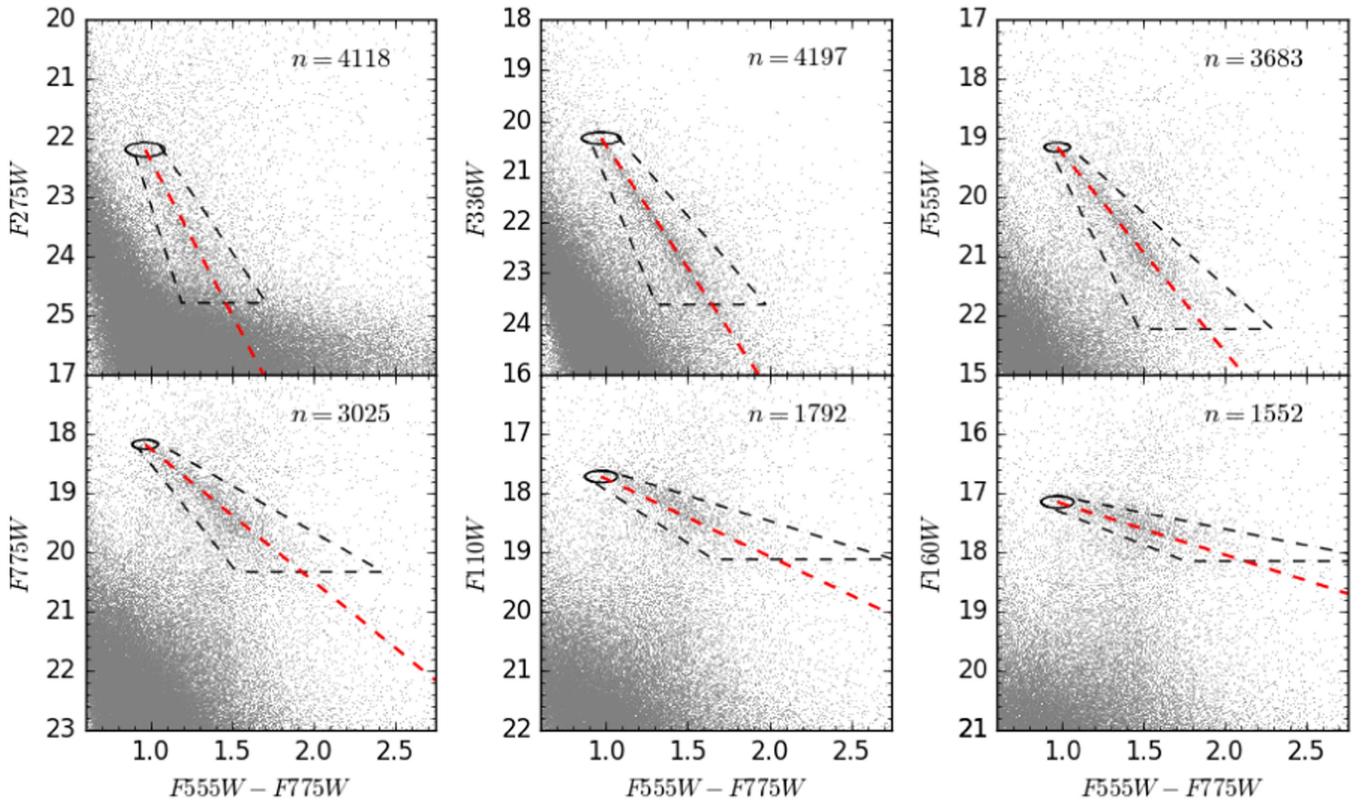


Figure 7. LMC 30 Dor CMDs from the HTTP survey with a focus on the RC. See Figure 6 for a detailed description of the features on the CMDs.

Table 4
SMC SMIDGE Extinction Curve Results

λ (Å)	λ^{-1} (μm)	Band Combination	R_{λ}
2359	4.24	$A_{225}/(A_{475}-A_{814})$	5.59 ± 0.23
2704	3.70	$A_{275}/(A_{475}-A_{814})$	4.95 ± 0.19
3355	2.98	$A_{336}/(A_{475}-A_{814})$	3.56 ± 0.13
4747	2.10	$A_{475}/(A_{475}-A_{814})$	2.65 ± 0.11
5581	1.79	$A_{550}/(A_{475}-A_{814})$	2.34 ± 0.10
8024	1.25	$A_{814}/(A_{475}-A_{814})$	1.72 ± 0.09
11534	0.87	$A_{110}/(A_{475}-A_{814})$	1.32 ± 0.08
15369	0.65	$A_{160}/(A_{475}-A_{814})$	1.13 ± 0.07

Table 5
LMC 30 Doradus Extinction Curve Results

λ (Å)	λ^{-1} (μm)	Band Combination	R_{λ}	$R_{\lambda}\text{DM16}^a$
2704	3.70	$A_{275}/(A_{555}-A_{775})$	5.28 ± 0.32	5.15 ± 0.38
3355	2.98	$A_{336}/(A_{555}-A_{775})$	4.83 ± 0.32	4.79 ± 0.19
5308	1.88	$A_{555}/(A_{555}-A_{775})$	3.16 ± 0.30	3.35 ± 0.15
7647	1.31	$A_{775}/(A_{555}-A_{775})$	2.28 ± 0.20	2.26 ± 0.14
11534	0.87	$A_{110}/(A_{555}-A_{775})$	1.30 ± 0.24	1.41 ± 0.15
15369	0.65	$A_{160}/(A_{555}-A_{775})$	0.83 ± 0.13	0.95 ± 0.18

Note.

^a Note that **DM16** call this value R and not R_{λ} .

for the galaxy from RC stars, we find the minimum χ^2 value by comparing our measured R_{λ} values to those for modeled reddened RCs with varying line-of-sight depths and input extinction curves. A similar measurement is performed for our LMC extinction curve results. Our results suggest that the

observed SMC and LMC RC extinction curves indicate a significant depth along the line of sight in both galaxies. For the SMC, we find the χ^2_{\min} at a line-of-sight depth of $10 \text{ kpc} \pm 2 \text{ kpc}$ at a 90% confidence level for the SMC Bar extinction curve. Comparing the SMIDGE extinction curve with other curves (**G03**'s SMC Bar [$R_V = 2.74$], SMC Wing [AzV 456, $R_V = 2.05$], LMC 2 Supershell [$R_V = 2.76$], LMC Average [$R_V = 3.41$], **F99**'s MW $R_V = 3.1$ and MW $R_V = 5.5$, and with **WD01**'s curves), we find that the newly derived SMC extinction curve compares almost equally well with both the **G03** SMC Bar and SMC Wing extinction curves (see left panels of Figure 9). To differentiate between the two, our future work will use UV-bright stars to study the F225W extinction, which will eliminate issues with the red leak.

For the LMC 30 Dor region we obtain a χ^2_{\min} at a line-of-sight depth of $5 \text{ kpc} \pm 1 \text{ kpc}$ at the 90% confidence level. Comparing the LMC extinction curve with the above curves, we find that this curve similarly does not favor a single observed extinction curve, but that it instead can be well described by either the **G03** LMCave extinction curve ($R_V = 3.41$) or the **F99** MW $R_V = 3.1$ curve. The latter would suggest a $7 \pm 1 \text{ kpc}$ line-of-sight depth.

4.2. Comparison to Other Extinction Curve Shape Measurements

Extinction curves in the SMC and the LMC have been measured spectroscopically by Gordon & Clayton (1998), **G03**, Maíz Apellániz & Rubio (2012), and Maíz Apellániz et al. (2014). **G03** derive extinction curves for the SMC and the LMC via the pair method using ultraviolet spectroscopy and optical and near-infrared photometry. They base their conclusions on five stars in the SMC, four of which are in the SMC

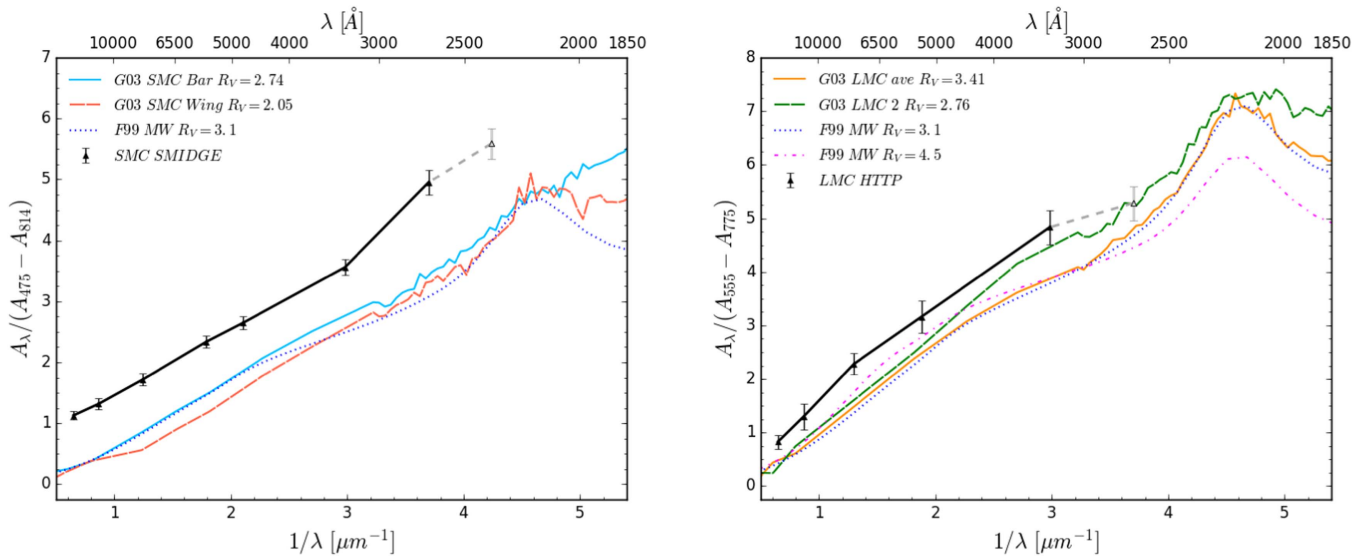


Figure 8. Left: SMC SMIDGE extinction curve, plotted in black. For comparison, the Gordon et al. (2003, G03) SMC Bar and SMC Wing curves and the Fitzpatrick (1999, F99) MW $R_V = 3.1$ curves normalized to SMIDGE wavelengths are shown as well. Right: 30 Dor LMC extinction curve. The LMC average and LMC 2 G03 curves and the F99 MW $R_V = 3.1$ and $R_V = 4.5$ curves are plotted as well. We conclude that the observed offsets in both the SMC and the LMC curves (the latter also noted by DM16) are a result of the significant depth along the line of sight of both galaxies (see Section 3.2).

Bar, producing an average $R_V = 2.74 \pm 0.13$, and one star in the SMC wing with $R_V = 2.05 \pm 0.17$. They also measure an average LMC 2 Supershell (“LMC2”) $R_V = 2.76 \pm 0.09$ for 9 stars and an LMC Average $R_V = 3.41 \pm 0.06$ for 10 stars. These extinction curves are plotted in Figure 8 for comparison with the extinction curve results from this study. We observe a general consistency in our results for the shape of the SMC and LMC extinction curves with the shape of the G03 curves for wavelengths longward of F225W’s. At the same time, we note the offset between the two sets of curves, which we attribute to the effect of the depth of the two galaxies along the line of sight described in Section 3.2. We cannot make a strong statement about the UV portion of the curve, as we are limited by photometric effects when using RC stars.

DM14a, DM14b, and DM16 use UV–IR multiband *HST* photometry to examine 30 Doradus in the LMC. They find an offset between their results and the results of G03 and the canonical Galactic extinction curves due to RC reddening vector slopes that are considerably steeper than existing measurements. Our measurements reproduce DM16’s results. The authors attribute their results to the presence of “gray” extinction at optical wavelengths due to the vertical offset of their curves from the Galactic and G03 curves. Our model explains this effect as the result of the line-of-sight depth of the LMC, where the extinction curve is well-reproduced by the G03 LMC average $R_V = 3.41$ extinction curve with a 5 kpc line-of-sight depth (see Figure 9).

Maíz Apellániz & Rubio (2012) use UV spectroscopy to obtain the extinction for four stars in the SMC quiescent cloud B1-1 and NIR/optical photometry to obtain the extinction curve for the five SMC stars studied by G03. They conclude a significant variation from star to star in the extinction curve for the SMC B1-1 stars, particularly in the strength of the 2175 Å bump. Their results may imply that their sources are sampling ISM environments with a different dust composition. In the following section we discuss the type of environment probed

by the SMIDGE region and conclude that our results are most likely dominated by the diffuse ISM. However, we currently do not have a conclusive result about the strength of the 2175 Å bump due to the limitations of our RC photometry.

Maíz Apellániz et al. (2014) use spectroscopy and NIR and optical photometry of O and B stars to derive the extinction curve inside 30 Doradus. They find an R_V equivalent that is also larger than the R_V suggested by Galactic or G03 extinction curves. Although our results for 30 Dor agree with the authors’ $R_V = 4.5$ curve at optical wavelengths when the curves are expressed in $E(B - V)$ instead of $E(F555W - F775W)$ using spline interpolation, our extinction curve is better reproduced at NIR wavelengths by the G03 LMC average $R_V = 3.41$ curve with a 5 kpc line-of-sight depth. The latter is also the case when the curves are normalized to A_V . We obtain very similar results when we compare the DM16 curve (with values in the last column of Table 5) to the Maíz Apellániz et al. (2014) curve.

Recent work by Hagen et al. (2017) uses SMC UV, optical, and IR data integrated into 200” regions to measure the attenuation curve of the SMC. They find a 2175 Å bump in most of the galaxy and a dust curve that is steeper than the Galactic curve. We note that their study measures the attenuation curve (i.e., the combined effects of extinction, scattering, and geometry; see Calzetti et al. 1994). Our results, which are extinction curves, are not directly comparable to this study.

RC stars have been extensively used as a distance indicator to objects within the MW and nearby galaxies (Cannon 1970; Girardi & Salaris 2001; Bovy et al. 2014; see also Girardi 2016, and references therein). Within the Galaxy in particular, they have been used to indicate the distance to the Galactic center (Paczynski & Stanek 1998; Alves 2000; Francis & Anderson 2014) and to open clusters (Percival & Salaris 2003). Distributions of stellar distances in the Magellanic Clouds have been measured with RR Lyrae and Cepheids (Haschke et al. 2012; Subramanian & Subramanian 2012;

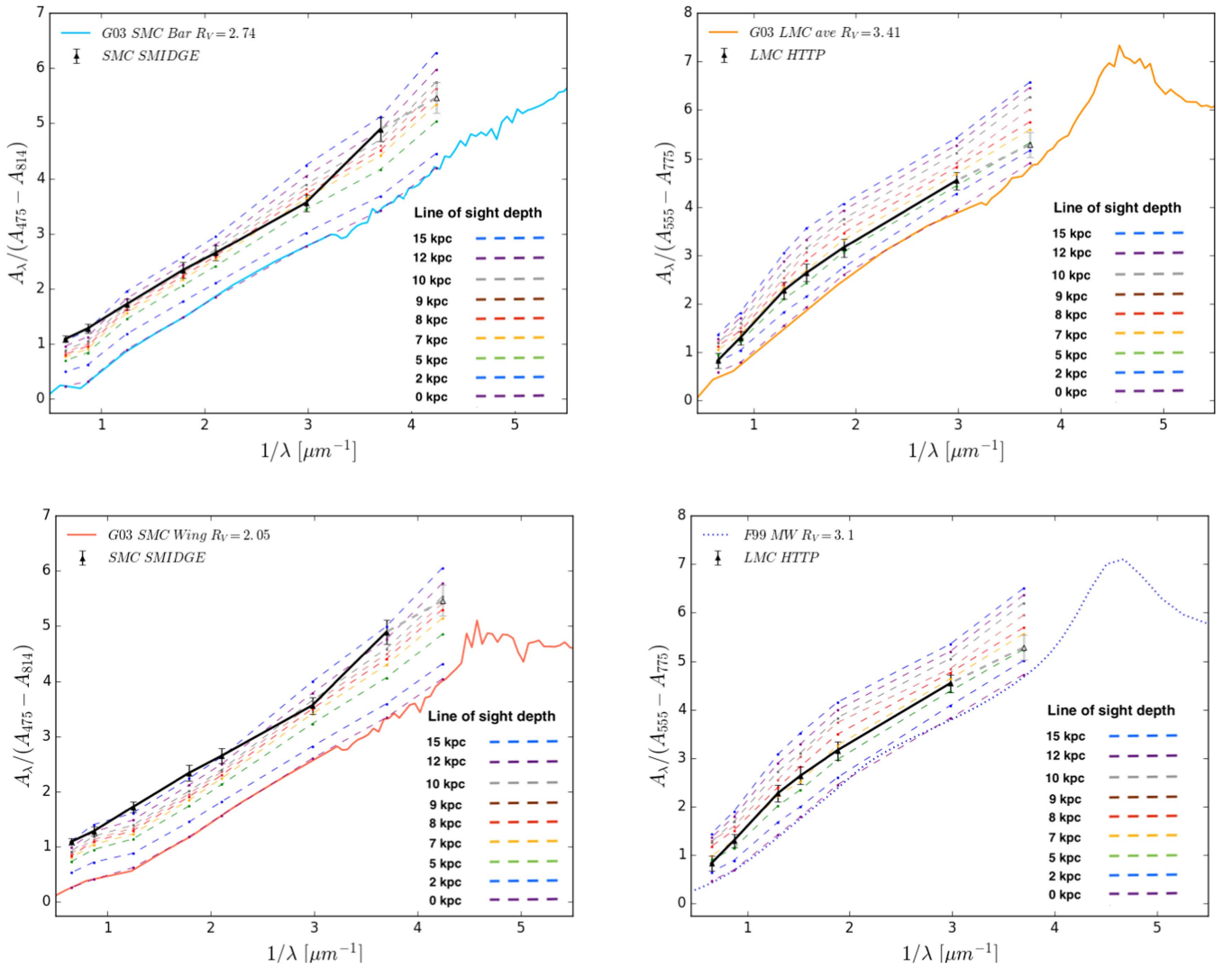


Figure 9. Effect of the line-of-sight depth of the SMC and the LMC on the SMC and LMC extinction curves of G03 and the MW $R_V = 3.1$ curve of F99, showing the offset in the presence of galactic depth between 0 and 15 kpc. The SMC SW Bar extinction curve found in this study and plotted in black in the two panels on the left indicates a line-of-sight depth of 10 ± 2 kpc when compared to the G03 SMC Bar curve and 12 ± 2 kpc when compared to the G03 SMC Wing curve. The LMC 30 Doradus extinction curve is plotted in black in the panels on the right and indicates that it is probing a region with a line-of-sight depth of 5 ± 1 kpc when compared to the G03 LMC average curve and 7 ± 1 kpc when compared to the F99 MW $R_V = 3.1$ curve. Details of this analysis are in Section 4.1.

Jacyszyn-Dobrzanieckas et al. 2016, 2017; Scowcroft et al. 2016), and with RC stars (Subramanian et al. 2017). Our results in Section 4.1 indicating that the SMC has a depth of ~ 10 kpc along the line of sight and that the LMC’s depth is ~ 5 kpc are generally consistent with distances derived from the Cepheids and RR Lyrae studies above.

5. Discussion

We present measurements of the average extinction curve shape in the southwest bar region of the SMC covering an area of 100×200 pc using RC stars. Our results indicate an extinction curve consistent with measurements from UV spectroscopy performed by G03. The significantly elongated structure of the SMC along the line of sight causes a perceived steepening of the reddening vector that, if not accounted for, would give the appearance of an extinction curve with a “gray” component. The latter is the conclusion of DM16 for the extinction curve of the 30 Doradus nebula in the LMC, which

they attribute to the presence of an additional component due to gray dust. We conclude that gray extinction is not necessary to explain the observations in the SMC and the LMC when one accounts for the depth of the stellar distribution along the line of sight.

There are several implications of our measurements. By sampling a relatively large region of the ISM in the SMC, we can compare our averaged extinction curve results to measurements derived using the pair method targeting individual stars. We do this while noting that, compared to the pair method, the technique we use presents a number of advantages, one of which is that by observing RC stars on a CMD we do not need to know the location of the dust since we are taking an average measure of dust properties. One of the pair method’s major limitations comes from having to carefully select stars in regions containing a significant amount of dust. At the same time, due to photometric limitations resulting from *HST*’s red leak and the faintness of the stars in F225W, the RC technique

we use in this paper does not allow us to have a strong handle on the strength of the 2175 Å bump or the far-UV rise.

One comparison we can make is with the work of G03, who studied SMC extinction with the pair method. An interpretation of the similarity between our results and those of G03 may be that over a relatively large area in the SMC there is little variation in the extinction curve shape. Another possibility is that both studies are sampling the same ISM phases. The dust probed with O- and B-type stars such as those from the UV spectroscopy sightlines of G03 is generally assumed to be located in the diffuse envelopes of molecular clouds, which would bias the extinction curves toward regions of star formation dominated by grain growth. However, the G03 SMC Bar A_V extinctions of 0.35–0.68 indicate that these sightlines are probing the diffuse ISM, or at least regions where coagulation and grain growth are unlikely to have happened.

To address the hypothesis that both sets of extinction curves are probing the same ISM phases (e.g., diffuse atomic or molecular gas), we assess the type of environment the SMIDGE survey area covers by calculating the fraction of stars along lines of sight that have abundant molecular gas. Using APEX ^{12}CO (2–1) mapping of the SW Bar at 28'' resolution (A. Bolatto 2017, private communication), we make a conservative cut at $I_{\text{CO}} = 1 \text{ K km s}^{-1}$ to define molecular regions. We find that 23% of the RC stars are found toward such regions, indicating that our new average extinction curves are dominated by diffuse material. It remains a possibility that both G03 and our work are sampling mainly the diffuse ISM, rather than molecular gas where grain growth may occur. In future work we will investigate the change of the extinction curve with ISM phase using the full stellar populations available from SMIDGE.

Another implication of our study is that extinction in the SMC and the LMC can be explained without the need to invoke “gray” extinction as suggested by DM14a, DM14b, and DM16 for the LMC. If there were gray dust, the latter suggest that the reason may be the selective addition of fresh large grains due to SN II explosions in 30 Dor. If recent supernovae were the cause, this could suggest a bias toward gray extinction for galaxies with high SFRs. Gray dust also has implications for studies of the cosmological expansion with supernovae, as their faintness could be interpreted as extinction without much reddening, which would invariably impact inferring distances on cosmological scales. Observationally there are demonstrations of the presence of gray extinction (Strom et al. 1971; Dunkin & Crawford 1998; Gall et al. 2014). However, our study concludes that extinction curves in the LMC can be explained without the need for an extra “gray” component of the dust, thus removing the argument for supernova dust production modifying the extinction curve.

6. Conclusions

We use CMDs based on SMIDGE *HST* multiband photometry to measure the slope of the reddening vector of red clump stars in the southwest bar of the Small Magellanic Cloud in order to derive the extinction curve shape in the region. After noting that the depth along the line of sight of the SMC has a significant bearing on extinction curve shape results using this method, we model this effect to understand its impact on our

results. When we properly account for the line-of-sight depth and analyze its effect on extinction curves, we conclude that the effect is significant and tends to give the appearance of steeper reddening vector slopes, which in turn produce what appears to be gray extinction. Motivated by recent extinction curve shape results for 30 Dor in the LMC by DM14a and DM16, who use the same RC method and also report an offset, we perform the same analysis on 30 Dor in the LMC.

Our conclusions for the optical and NIR portions of the extinction curve shape in both the SMC and the LMC are consistent with previous work such as the analysis of G03 using spectroscopic measurements. Since depth effects in both galaxies produce an offset in the extinction curve due to a perceived steepening of the reddening vector, we conclude that it is the shape of the G03 curves that our extinction curves match rather than a specific R_V value. Our recommendation to correct for dust extinction for individual objects is therefore to use the extinction curves derived by G03. Correcting for dust extinction when using a full stellar population, however, calls for the need to account for the depth of the SMC and the LMC. Additionally, we show that it does not have to be the case that gray extinction is responsible for the offset in the LMC 30 Dor extinction curve, as DM14a and DM16 conclude, but that rather one needs to account for the depth along the line of sight when using methods relying on stellar distances to determine the extinction curve shape. Future work aims at modeling the effect of extinction on all CMD features rather than simply on a generic RC. Such an analysis will provide a way to understand the more subtle effects of dust on the extinction curve shape.

We thank the referee, whose comments helped improve this work. Support for this work was provided by NASA through grant no. HST-GO-13659 from the Space Telescope Science Institute, which is operated by AURA, Inc., under NASA contract NAS5-26555. These observations are associated with program no. GO-13659. This work is based on observations made with the NASA/ESA *Hubble Space Telescope*. The research made extensive use of NASA’s Astrophysics Data System bibliographic services. This research made use of Astropy, a community-developed core Python package for astronomy (Astropy Collaboration et al. 2013), NumPy (Van Der Walt et al. 2011), and Matplotlib (Hunter 2007). Additionally, the study made use of two dust extinction tools—`pyextinction` created by Morgan Fouesneau and hosted at <https://github.com/mfouesneau/pyextinction>, and the Bayesian Extinction and Stellar Tool created by Karl Gordon (Gordon et al. 2016, BEAST) and hosted at <https://github.com/BEAST-Fitting/beast>.

Appendix Model Sensitivity Tests

A number of factors influence the calculated slope of the reddening vector using the RC method. We perform tests to determine how this slope varies with changing parameters such as

1. the width of the selection boundary around the RC,
2. the intrinsic width of the unreddened RC, and
3. the unreddened RC location.

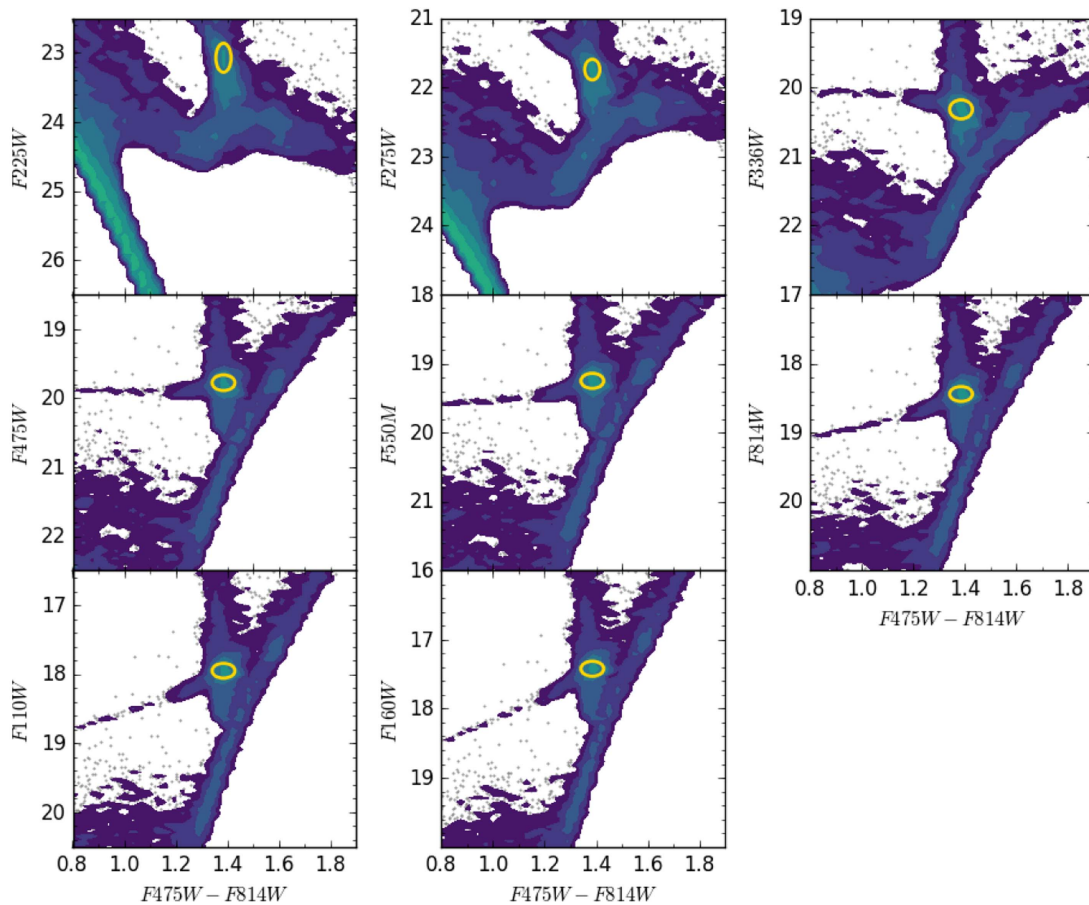


Figure 10. SMC synthetic CMDs generated to determine the location of the unreddened RC (yellow ellipse, with values indicated in Table 2) as described in Section 3.2 and Figure 3.

Synthetic CMDs for all F475W-F814W color-magnitude combinations are shown in Figure 10. We extract the location of the unreddened RC (designated by a yellow ellipse) from these CMDs based on parameters specified in Section 3.2. We specify the width of the reddened RC selection region by first calculating the feature’s approximate slope and then adding and subtracting a percent to this slope to define the slopes of the two boundaries tangent and extending redward of the unreddened RC ellipse (see Section 3.4, top). To understand the behavior of the resulting reddening vector slope as we define these tangent boundaries, we vary the percent added and subtracted to the approximate slope between 0% and 40% (Figure 11, top panel). A 0% variation would mean that the reddened RC boundary encompasses a relatively narrow region defined by two tangents to the ellipse of the unreddened RC running parallel to the approximate slope. A 40% variation, on the other hand, means that the RC boundary encompasses a relatively large cone-shaped region whose width is set by ellipse tangents with slopes $\pm 40\%$ of the approximate slope. These selection boundaries are illustrated in Figure 12, where we more realistically depict the $\pm 5\%$ case rather than the 0% case.

We also explore the effect the intrinsic width of the unreddened RC has on the slope of the reddening vector (Figure 11, middle). This width is present due to the age and

metallicity uncertainties of the RC discussed in Section 3.2. We observe the effect of a changing width on our results by varying σ_{col} from 0.06 mag (see Table 2) to twice this value.

Lastly, to allow for a potential ambiguity in the unreddened position of the RC in magnitude due to the distance effect discussed in Section 3.2, we let the centroid of the RC distance modulus vary by 0.15 mag to simulate the effect of a distance shift away from 62 kpc ($\mu = 18.96$; Scowcroft et al. 2016) by ~ 4.5 kpc (Figure 11, bottom).

We observe that the variation in both the approximate reddening vector slope and the width of the unreddened RC produces relatively constant results that fall within the overall uncertainties. The slope of F225W is most susceptible to variation due to the steepness and faintness of the RC at this wavelength. Our third sensitivity test that varies the magnitude position of the unreddened RC by ± 0.15 mag away from the values given in Table 2 results in a calculated reddening vector slope with a similar offset across each CMD. For the range of magnitude variations we find a χ^2_{min} that supports a significant line-of-sight depth (between 7 and 15 kpc). We therefore conclude that a variation in the unreddened RC zero-point does not remove the necessity to account for a substantial galactic depth when analyzing the extinction curve using the RC method.

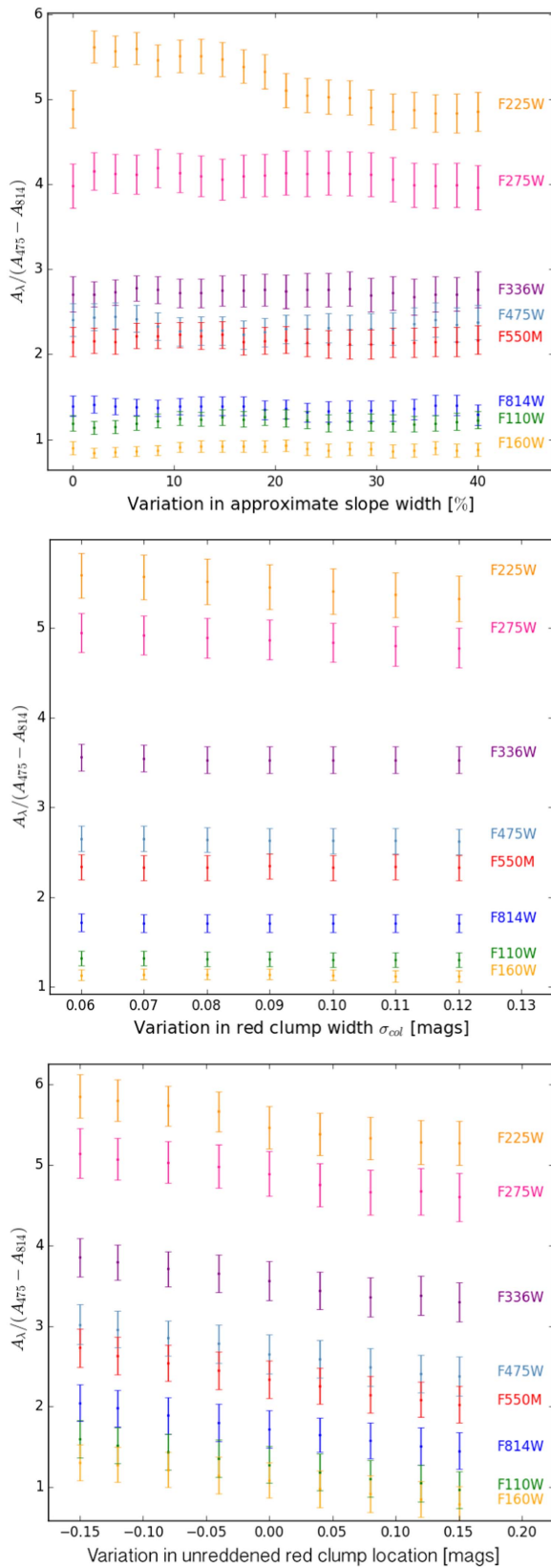


Figure 11. Sensitivity of the calculated reddening vector slope to three parameters. The top panel shows the sensitivity to the approximate slope that determines the width of the reddened RC selection region. The middle panel tests the sensitivity to the intrinsic width in color of the unreddened RC. The bottom panel illustrates the sensitivity to the unreddened RC location.

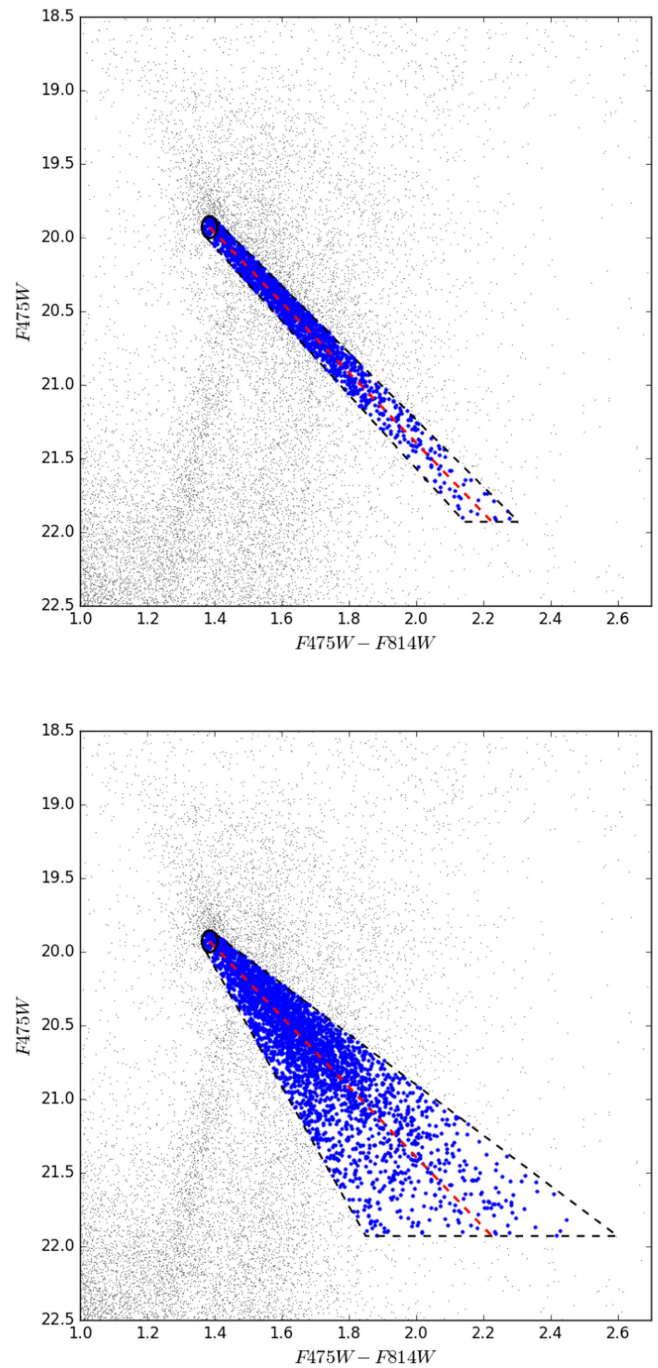


Figure 12. RC selection with variations in the approximate reddening vector slope to determine the effect of the selection on the slope calculation. The top panel shows a selection box corresponding to a $\pm 5\%$ variation in the approximate slope; the bottom panel shows the selection after a $\pm 40\%$ variation is added. The blue points represent the highlighted reddened RC stars inside the selection region.


ORCID iDs

Petia Yanchulova Merica-Jones  <https://orcid.org/0000-0002-9912-6046>

Karin M. Sandstrom  <https://orcid.org/0000-0002-4378-8534>

L. Clifton Johnson  <https://orcid.org/0000-0001-6421-0953>

Julianne Dalcanton  <https://orcid.org/0000-0002-1264-2006>

Andrew E. Dolphin  <https://orcid.org/0000-0001-8416-4093>
 Karl Gordon  <https://orcid.org/0000-0001-5340-6774>
 Julia Roman-Duval  <https://orcid.org/0000-0001-6326-7069>
 Daniel R. Weisz  <https://orcid.org/0000-0002-6442-6030>
 Benjamin F. Williams  <https://orcid.org/0000-0002-7502-0597>

References

- Alves, D. R. 2000, *ApJ*, **539**, 732
 Astropy Collaboration, Robitaille, T. P., Tollerud, E. J., et al. 2013, *A&A*, **558**, A33
 Bovy, J., Nidever, D. L., Rix, H.-W., et al. 2014, *ApJ*, **790**, 127
 Bressan, A., Marigo, P., Girardi, L., et al. 2012, *MNRAS*, **427**, 127
 Caldwell, J. A. R., & Coulson, I. M. 1986, *MNRAS*, **218**, 223
 Calzetti, D., Kinney, A. L., & Storchi-Bergmann, T. 1994, *ApJ*, **429**, 582
 Cannon, R. D. 1970, *MNRAS*, **150**, 111
 Cardelli, J. A., Clayton, G. C., & Mathis, J. S. 1989, *ApJ*, **345**, 245
 Cardelli, J. A., Sembach, K. R., & Mathis, J. S. 1992, *AJ*, **104**, 1916
 Cartledge, S. I. B., Clayton, G. C., Gordon, K. D., et al. 2005, *ApJ*, **630**, 355
 Chen, Y., Bressan, A., Girardi, L., et al. 2015, *MNRAS*, **452**, 1068
 Cignoni, M., Sabbi, E., Nota, A., et al. 2009, *AJ*, **137**, 3668
 Clayton, G. C., & Martin, P. G. 1985, *ApJ*, **288**, 558
 Dalcanton, J. J., Fouesneau, M., Hogg, D. W., et al. 2015, *ApJ*, **814**, 3
 De Marchi, G., & Panagia, N. 2014, *MNRAS*, **445**, 93
 De Marchi, G., Panagia, N., & Girardi, L. 2014, *MNRAS*, **438**, 513
 De Marchi, G., Panagia, N., Sabbi, E., et al. 2016, *MNRAS*, **455**, 4373
 Dolphin, A. E. 2000, *PASP*, **112**, 1383
 Dolphin, A. E. 2002, *MNRAS*, **332**, 91
 Dressel, L. 2014, Wide Field Camera 3 Instrument Handbook, Version 6.0 (Baltimore, MD: STScI), <http://documents.stsci.edu/hst/acs/documents/handbooks/cycle22/cover.html>
 Dufour, R. J. 1984, in IAU Symp. 108, Structure and Evolution of the Magellanic Clouds, ed. S. van den Bergh & K. S. de Boer (Dordrecht: D. Reidel), 353
 Dunkin, S. K., & Crawford, I. A. 1998, *MNRAS*, **298**, 275
 Fitzpatrick, E. L. 1985, *ApJ*, **299**, 219
 Fitzpatrick, E. L. 1999, *PASP*, **111**, 63
 Florsch, A., Marcout, J., & Fleck, E. 1981, *A&A*, **96**, 158
 Francis, C., & Anderson, E. 2014, *MNRAS*, **441**, 1105
 Gall, C., Hjorth, J., Watson, D., et al. 2014, *Natur*, **511**, 326
 Galliano, F., Madden, S. C., Jones, A. P., Wilson, C. D., & Bernard, J.-P. 2005, *A&A*, **434**, 867
 Gardiner, L. T., & Hatzidimitriou, D. 1992, *MNRAS*, **257**, 195
 Gardiner, L. T., & Hawkins, M. R. S. 1991, *MNRAS*, **251**, 174
 Girardi, L. 2016, *ARA&A*, **54**, 95
 Girardi, L., & Salaris, M. 2001, *MNRAS*, **323**, 109
 Glatt, K., Gallagher, J. S., III, Grebel, E. K., et al. 2008, *AJ*, **135**, 1106
 Gordon, K. D., & Clayton, G. C. 1998, *ApJ*, **500**, 816
 Gordon, K. D., Clayton, G. C., Misselt, K. A., Landolt, A. U., & Wolff, M. J. 2003, *ApJ*, **594**, 279
 Gordon, K. D., Fouesneau, M., Arab, H., et al. 2016, *ApJ*, **826**, 104
 Hagen, L. M. Z., Siegel, M. H., Hoversten, E. A., et al. 2017, *MNRAS*, **466**, 4540
 Haschke, R., Grebel, E. K., & Duffau, S. 2012, *AJ*, **144**, 107
 Hatzidimitriou, D., & Hawkins, M. R. S. 1989, *MNRAS*, **241**, 667
 Hennebelle, P., & Falgarone, E. 2012, *A&ARv*, **20**, 55
 Hill, A. S., Benjamin, R. A., Kowal, G., et al. 2008, *ApJ*, **686**, 363
 Hunter, J. D. 2007, *CSE*, **9**, 90
 Isobe, T., Feigelson, E. D., Akritas, M. G., & Babu, G. J. 1990, *ApJ*, **364**, 104
 Jacyszyn-Dobrzyniecka, A. M., Skowron, D. M., Mróz, P., et al. 2016, *AcA*, **66**, 149
 Jacyszyn-Dobrzyniecka, A. M., Skowron, D. M., Mróz, P., et al. 2017, *AcA*, **67**, 1
 Kainulainen, J., Beuther, H., Henning, T., & Plume, R. 2009, *A&A*, **508**, L35
 Kapakos, E., & Hatzidimitriou, D. 2012, *MNRAS*, **426**, 2063
 Kroupa, P. 2001, *MNRAS*, **322**, 231
 Kurt, C. M., Dufour, R. J., Garnett, D. R., et al. 1999, *ApJ*, **518**, 246
 Lee, J.-K., Rolleston, W. R. J., Dufton, P. L., & Ryans, R. S. I. 2005, *A&A*, **429**, 1025
 Lequeux, J., Maurice, E., Prevot-Burnichon, M.-L., Prevot, L., & Rocca-Volmerange, B. 1982, *A&A*, **113**, L15
 Maíz Apellániz, J., Evans, C. J., Barbá, R. H., et al. 2014, *A&A*, **564**, A63
 Maíz Apellániz, J., & Rubio, M. 2012, *A&A*, **541**, A54
 Massa, D., Savage, B. D., & Fitzpatrick, E. L. 1983, *ApJ*, **266**, 662
 Monson, A. J., Freedman, W. L., Madore, B. F., et al. 2012, *ApJ*, **759**, 146
 Muller, E., Staveley-Smith, L., Zealey, W., & Stanimirović, S. 2003, *MNRAS*, **339**, 105
 Nataf, D. M., Gould, A., Fouqué, P., et al. 2013, *ApJ*, **769**, 88
 Nidever, D. L., Monachesi, A., Bell, E. F., et al. 2013, *ApJ*, **779**, 145
 Noll, S., & Pierini, D. 2005, *A&A*, **444**, 137
 Paczyński, B., & Stanek, K. Z. 1998, *ApJL*, **494**, L219
 Percival, S. M., & Salaris, M. 2003, *MNRAS*, **343**, 539
 Prevot, M. L., Lequeux, J., Prevot, L., Maurice, E., & Rocca-Volmerange, B. 1984, *A&A*, **132**, 389
 Rolleston, W. R. J., Dufton, P. L., McErlean, N. D., & Venn, K. A. 1999, *A&A*, **348**, 728
 Rolleston, W. R. J., Venn, K., Tolstoy, E., & Dufton, P. L. 2003, *A&A*, **400**, 21
 Rubele, S., Girardi, L., Kerber, L., et al. 2015, *MNRAS*, **449**, 639
 Russell, S. C., & Dopita, M. A. 1992, *ApJ*, **384**, 508
 Sabbi, E., Anderson, J., Lennon, D. J., et al. 2013, *AJ*, **146**, 53
 Sabbi, E., Gallagher, J. S., Tosi, M., et al. 2009, *ApJ*, **703**, 721
 Sabbi, E., Lennon, D. J., Anderson, J., et al. 2016, *ApJS*, **222**, 11
 Schlafly, E. F., Meisner, A. M., Stutz, A. M., et al. 2016, *ApJ*, **821**, 78
 Scowcroft, V., Freedman, W. L., Madore, B. F., et al. 2016, *ApJ*, **816**, 49
 Strom, K. M., Strom, S. E., & Yost, J. 1971, *ApJ*, **165**, 479
 Subramanian, S., Rubele, S., Sun, N.-C., et al. 2017, *MNRAS*, **467**, 2980
 Subramanian, S., & Subramaniam, A. 2009, *A&A*, **496**, 399
 Subramanian, S., & Subramaniam, A. 2012, *ApJ*, **744**, 128
 Tang, J., Bressan, A., Rosenfield, P., et al. 2014, *MNRAS*, **445**, 4287
 Trumpler, R. J. 1930, *PASP*, **42**, 214
 Van Der Walt, S., Colbert, S. C., & Varoquaux, G. 2011, *CSE*, **13**, 22
 Weingartner, J. C., & Draine, B. T. 2001, *ApJ*, **548**, 296
 Weisz, D. R., Dolphin, A. E., Skillman, E. D., et al. 2013, *MNRAS*, **431**, 364
 Welch, D. L., McLaren, R. A., Madore, B. F., & McAlary, C. W. 1987, *ApJ*, **321**, 162
 Welty, D. E., Xue, R., & Wong, T. 2012, *ApJ*, **745**, 173
 Williams, B. F., Lang, D., Dalcanton, J. J., et al. 2014, *ApJS*, **215**, 9